Monolithic Single-Frequency Laser on Thin-Film Lithium Niobate Platform by the Vernier Effect

Chao Sun(孙超)[1,2,3], Zhao-Xiang Liu(刘招祥)[1,2*], Jin-Ming Chen(陈锦明)[1,2], Min Wang(汪旻)[1,2], and Ya Cheng(程亚)[1,2,4,5,6]

[1]*The Extreme Optoelectromechanics Laboratory (XXL), School of Physics and Electronic Science, East China Normal University, Shanghai 200241, China*
[2]*State Key Laboratory of Precision Spectroscopy, East China Normal University, Shanghai 200062, China*
[3]*School of Arts and Sciences, Guangzhou Maritime University, Guangzhou 510725, China*
[4]*Hefei National Laboratory, Hefei 230088, China*
[5]*Shanghai Research Center for Quantum Sciences, Shanghai 201315, China*
[6]*Collaborative Innovation Center of Extreme Optics, Shanxi University, Taiyuan 030006, China*

(Received 4 December 2025; accepted manuscript online 6 January 2026)

We present a monolithic single-frequency microring laser utilizing Er^{3+}-doped thin film lithium niobate (TFLN) on insulator. The device is fabricated employing a dual-cavity architecture, in which two microring resonators are nested through two pulley coupling regions and share a common semicircular cavity. The single-frequency laser achieves a peak output power of 146 μW, with a side mode suppression ratio of 32 dB and slope efficiency of 0.7%, operating at a wavelength of 1530.85 nm, which leverages gain competition and the Vernier effect. Furthermore, the single-frequency laser emission can be selectively switched between 1530.85 nm and 1547.13 nm by a precise adjustment of the device's structural parameters. Our research establishes the foundation for a fully integrated multifunction TFLN system, which exhibits great potential applications in advancing optical computation, bio-chemical sensing, and signal processing.

DOI: 10.1088/0256-307X/43/2/020404 CSTR: 32039.14.0256-307X.43.2.020404

Thin film lithium niobate (TFLN) on insulator is a highly prospective material for the realization of next-generation, ultra-compact photonic integrated circuits (PICs), owing to its exceptional optical characteristics, including high nonlinear and electro-optic coefficients, pronounced piezoelectric and acousto-optic effects, significant photoelastic response, and a broad transparency window extending from the visible to the mid-infrared spectrum.[1–3] A diverse range of critical functional photonic devices has now been successfully demonstrated on the TFLN platform, including extremely efficient nonlinear frequency converters,[4,5] high-speed electro-optical modulation devices,[6,7] frequency combs,[8,9] and parametric optical oscillators.[10] However, the indirect bandgap nature of lithium niobate crystals fundamentally limits their potential for achieving efficient direct electroluminescence. Inspired by the success of Er^{3+}-doped fiber amplifiers, doping rare-earth ions (REIs) into TFLN represents a promising strategy to overcome its inherent limitations. Recent advances in doping REIs into TFLN have generated significant and broad interest, facilitating novel prospects for the advancement of superior-performance on-chip devices, including optical amplifiers, micro-cavity lasers, amplified spontaneous emission sources, and quantum memories.[11–17]

The development of Er^{3+}-doped TFLN has thereby facilitated the realization of diverse on-chip laser architectures, including micro-disk/ring resonator lasers, integrated Fabry–Perot (FP) cavity lasers, and photonic crystal nanolasers.[18–27] However, it is important to note that most laser systems reported to date exhibit multimode operation. Although waveguide amplifiers with large mode area can generate single-longitudinal-mode laser signals when sandwiched between fiber Bragg gratings,[28,29] this configuration does not allow for monolithic integration, which limits its practical application in PICs on TFLN. For the realization of multifunctional monolithic integration, there are several methods that can achieve the generation of single-mode laser signals. One approach is to design the waveguide structure of the micro-ring cavity appropriately to filter out higher-order modes, thereby achieving single-mode laser operation. Meanwhile, a single-longitudinal-mode laser may be achieved by strategically decreasing the microring radius to enhance the free spectral range (FSR), which effectively suppresses multi-mode oscillation.[30] Furthermore, a fundamental approach to achieving single-mode lasing involves either the implementation of gratings for mode selection or the harnessing of broken parity-time symmetry.[31–33] A FP resonator constructed based on the Sagnac loop reflector can also generate single-mode laser emission.[26,27] Another promising strategy to significantly enhance the FSR leverages the

*Corresponding author. Email: zxliu@phy.ecnu.edu.cn
© 2026 Chinese Physical Society and IOP Publishing Ltd. All rights, including for text and data mining, AI training, and similar technologies, are reserved.

Vernier effect by coupling multiple resonators of differing radii.[34–36] The modes supported by a resonator must satisfy the resonant condition: $2\pi R n_{\text{eff}} = m\lambda$, in which n_{eff} is the effective refractive index for the mode, R is the radius of the resonators, m is an integer, and λ is the resonant wavelength. The interplay of the Vernier effect and gain competition facilitated single-mode lasing in the experiment.

The current investigation presents a monolithic single-frequency microring resonator using a dual-cavity architecture, in which two microring resonators are nested through two pulley coupling regions and share a common semicircular cavity. The microring cavity employs a large mode area waveguide structure, which can store more pump power and achieve high output power. Relative to prior research,[24] two orders of magnitude have been added to the output power. Lasing at 1530.85 nm has been realized in the nested dual-cavity microring laser optically pumped at 1486 nm. The device demonstrates a threshold pump power of 5.1 mW, a peak output power of 146 μW, a side mode suppression ratio (SMSR) of 32 dB, and a corresponding slope efficiency of 0.7%. Enabled by an exact modification of the device's structural parameters, which leverages gain competition and the Vernier effect, the single-frequency laser emission can be selectively switched between 1530.85 nm and 1547.13 nm, with corresponding peak output powers of 146 μW and 47.5 μW, respectively. Our work establishes a critical step toward fully integrated, multifunctional photonic systems on TFLN, offering considerable promise for applications in high-performance optical computation, bio-chemical sensing, and advanced signal processing.

The device is fabricated on a Z-cut Er^{3+}-doped TFLN on insulator wafer, which is prepared via an ion-slicing technique (NanoLN, Jinan Jingzheng). The substrate comes from a bulk crystal of congruent Er^{3+}-doped lithium niobate that is generated using the Czochralski method. The concentration of Er^{3+}-doping in this crystal is around 0.5 mol%. The TFLN wafer structure comprises a 500 nm-thick top layer of lithium niobate, a 4.7 μm-thick buried oxide layer, and a 500 μm-thick silicon substrate at the bottom. The photolithography-assisted chemo-mechanical etching technique is employed to fabricate the device, following the procedure outlined in our previous work.[37,38]

The optical microscopy image of the fabricated nested dual-cavity microring resonator in Er^{3+}-doped TFLN is presented in Fig. 1(a). The device architecture features cavity a embedded inside cavity b, coupled via two pulley coupling regions. This configuration is designed to optimize the efficiency of the pulley coupler by ensuring phase matching between the microring resonator and the bus waveguide, thereby achieving maximum power transfer into cavity a.[39,40] To enhance the storage of pump power within cavity a, the waveguide width of cavity a is deliberately designed to be larger than that of cavity b in the experiment. The waveguide width of cavity b is established at 1 μm to achieve single-mode excitation, which

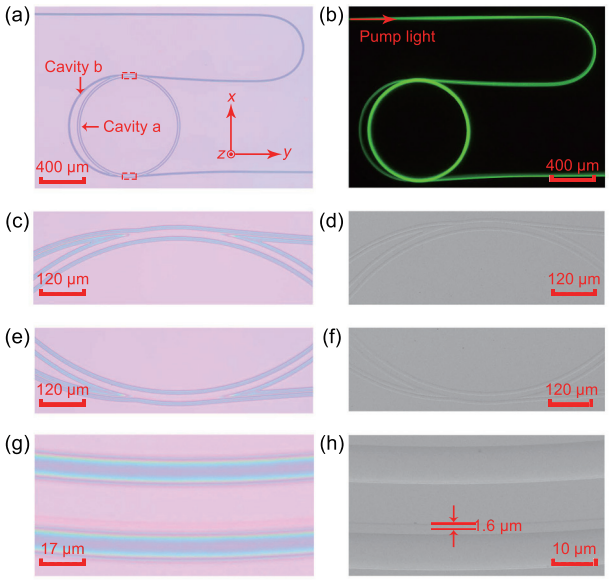

Fig. 1. (a) The optical microscope image of the Er^{3+}-doped TFLN nested dual-cavity microring resonator (the arrows indicate the TFLN crystallographic axes x, y, and z). (b) Captured green up-conversion fluorescence images of the nested dual-cavity microring resonator pumped by a 1486 nm laser. (c), (e), and (g) The optical microscopic, regionally zoomed images of the pulley-coupling region. (d), (f), and (h) High-resolution SEM images of the pulley-coupling region.

is identical to that of the adjacent bus waveguide. Figure 1(b) shows the strong green up-conversion fluorescence microscope image of the nested dual-cavity microring resonator under high-power pump laser excitation. Cavity a exhibits stronger fluorescence than cavity b, indicating that the pump light is successfully coupled and stored inside cavity a via two pulley coupling regions. The optical microscopy images of two pulley coupling regions are presented in Figs. 1(c) and 1(e), while the corresponding SEM images are shown in Figs. 1(d) and 1(f). The pulley coupling region is characterized by a coupling length of 100 μm. Figures 1(g) and 1(h) are optical microscopy image and scanning electron microscope (SEM) images that have magnified the pulley coupling region inside the dashed box of Fig. 1(a) locally. The pulley coupling region exhibits a gap of 1.6 μm, which is only faintly visible owing to the shallow etch depth attributed to the chemo-mechanical polishing process's poor selectivity.

The transmission spectrum of the Er^{3+}-doped TFLN nested dual-cavity microring resonator is acquired utilizing a tunable C-band external cavity diode laser (TOPTICA) in the experimental configuration illustrated in Fig. 2(a). The input light is first conditioned in polarization using a polarization controller and then efficiently coupled into the bus waveguide via a lensed fiber, ensuring that the intracavity field propagates exclusively in the TE_{00} mode. To ensure a consistent chip temperature, the device is mounted on a thermoelectric cooler. The bus waveguide's transmission spectrum can be measured through coupling the output light via a lensed fiber into a photodetector, and the resulting electrical signal is continuously

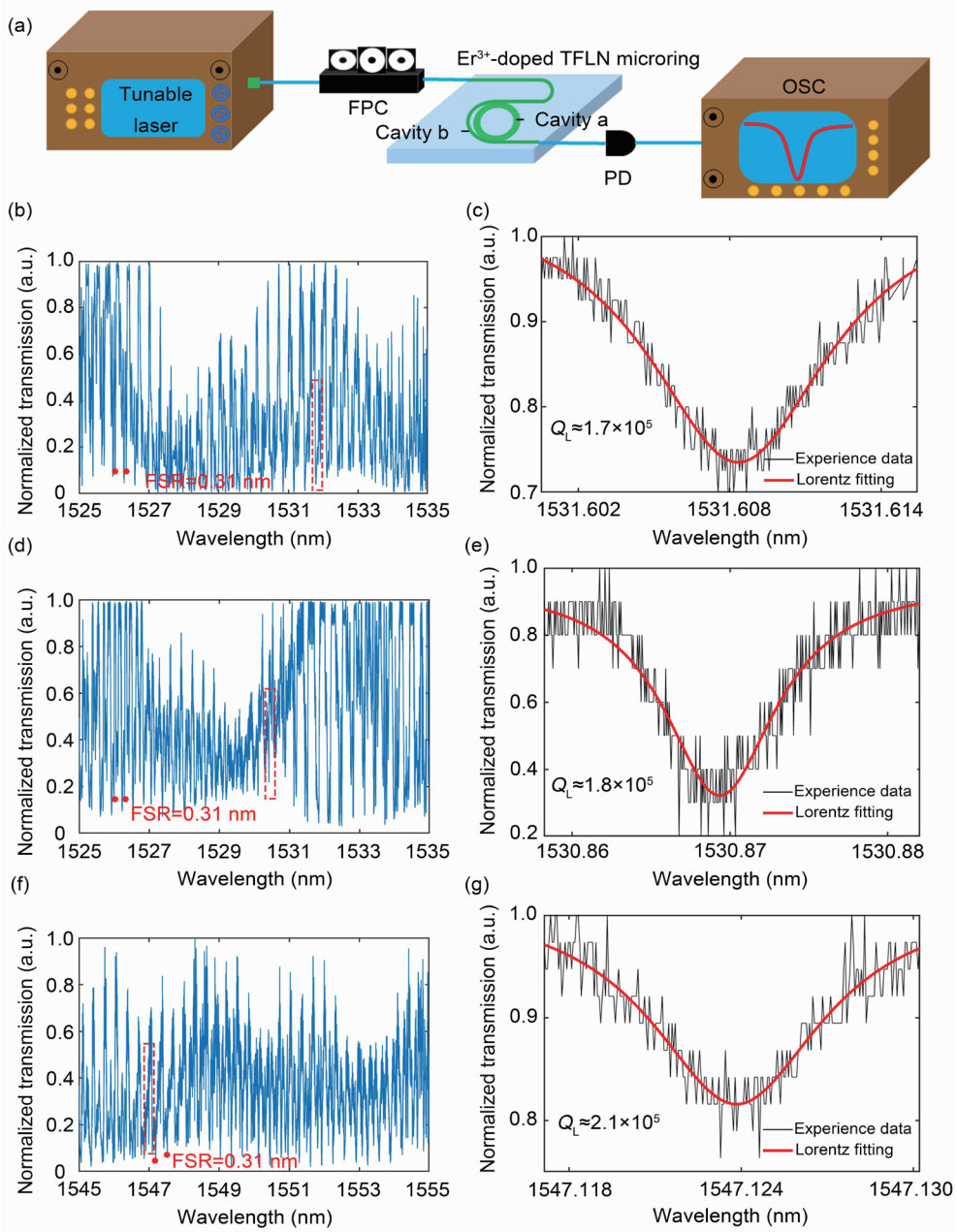

Fig. 2. (a) Schematic representation of the experimental configuration. PD, photodetector; FPC, fiber-based polarization controller; OSC, oscilloscope. Transmission spectrum of the Er^{3+}-doped TFLN nested dual-cavity microring resonator under different device structure parameters. (c), (e), and (g) Zoom-in of the red marked resonance mode in (b), (d), and (f).

recorded on an oscilloscope during wavelength scanning. The quality (Q) factors and FSRs in the vicinity of the laser wavelength are systematically investigated, as shown in Figs. 2(b)–2(g), for devices with three different sets of key geometric parameters. For the device characterized in Figs. 2(b) and 2(c), cavity b is fabricated to exceed cavity a in length by 40 µm, while the waveguide width of cavity a is fixed at 11.5 µm. As shown in Fig. 2(b), the transmission spectrum displays a high density of resonant modes spanning the wavelength range from 1500 nm to 1580 nm, featuring a FSR of 0.31 nm. Lorentzian fitting of the resonance near 1531.56 nm, shown in Fig. 2(b) by the red dashed box, revealed a Q factor of around 1.7×10^5, as detailed in Fig. 2(c). In the device configuration presented in Figs. 2(d) and 2(e), cavity b is intentionally constructed to be 40 µm longer than cavity a, while the waveguide width of the latter is narrowed to 5.5 µm. As illustrated in Fig. 2(d), a comparably dense array of resonant modes is observed, retaining an FSR of 0.31 nm. Through Lorentzian fitting of the resonance located at 1530.85 nm [Fig. 2(e)], a Q factor of approximately 1.8×10^5 is extracted. Finally, in the device corresponding to Figs. 2(f) and 2(g), the length difference between cavity b and cavity a is increased to 50 µm, while the waveguide width of cavity a is maintained at 5.5 µm. The resulting transmission spectrum, shown in Fig. 2(f), exhibits a

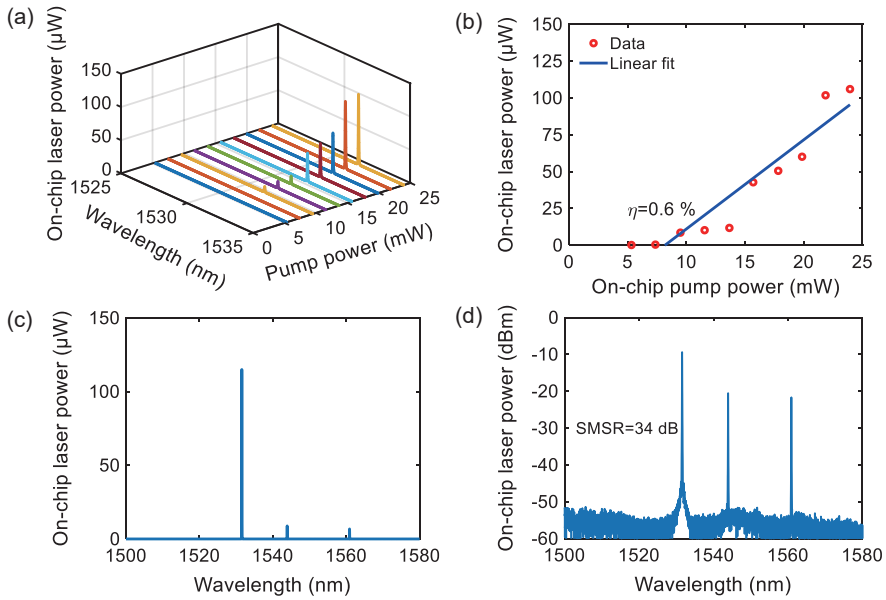

Fig. 3. (a) Spectral evolution of the Er^{3+}-doped TFLN nested dual-cavity microring resonator with increasing input pump powers. (b) On-chip output laser power as a function of input pump power. (c) and (d) Linear and logarithmic scales of the laser spectrum within the wavelength range of 1500–1580 nm for a pump power of 27.3 mW.

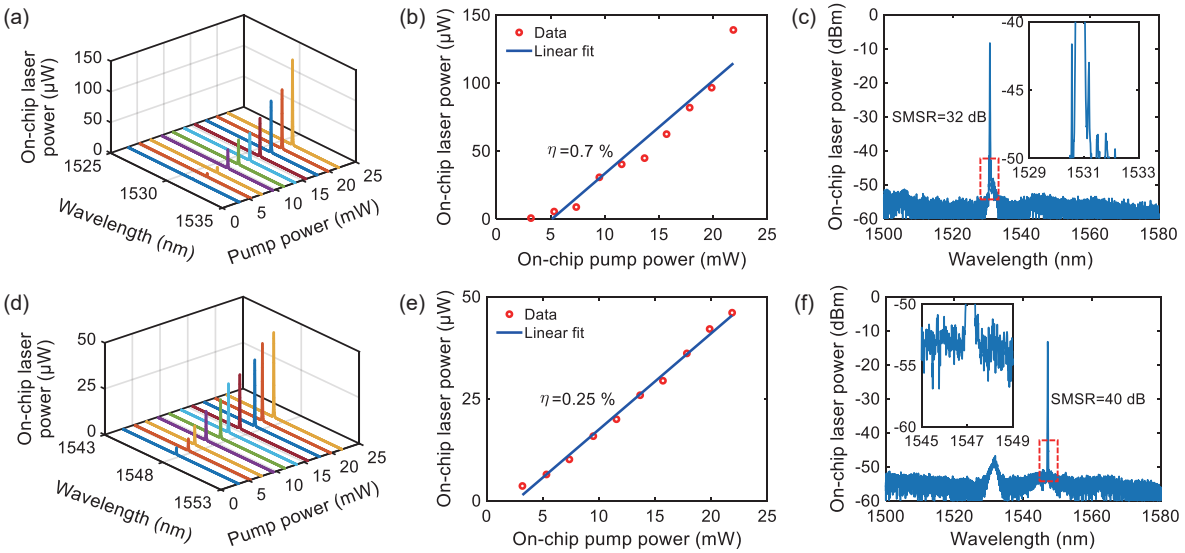

Fig. 4. (a) and (d) The spectral evolutions versus the input pump powers. (b) and (e) The on-chip output laser power vs. the input pump power. (c) and (f) The logarithmic scales of the laser spectrum within the wavelength range of 1500–1580 nm for a pump power of 22.9 mW.

consistently dense mode distribution with an unchanged FSR of 0.31 nm. Lorentzian fitting of the resonance at 1547.13 nm [Fig. 2(g)] yielded a high Q factor of approximately 2.1×10^5.

The device structure in Fig. 3 corresponds to that characterized in Fig. 2(b). The choice of a 1486 nm high-power laser diode is driven by its higher pumping efficiency relative to that at 980 nm, a result of its more favorable mode overlap.[12] The emitted laser signals are captured and examined using an optical spectrum analyzer with a resolution of up to 0.05 nm. Figure 3(a) presents a series of output lasing spectra, demonstrating a monotonic increase in the peak signal power with rising pump power. Figure 3(b) illustrates the relationship between output laser power and incident pump power, resulting in a slope efficiency of 0.6% and a lasing threshold of 8.1 mW. The device, which has a dominating lasing mode at 1531.56 nm with an SMSR of 34 dB, reaches a peak output power of 115 μW at a pump power of 27.3 mW, as seen in Figs. 3(c) and 3(d). Concurrently, the emission spectrum reveals additional lasing lines at 1543.92 nm and 1560.91 nm.

The laser performance under different device structural parameters is then investigated, as shown in Fig. 4, for the investigated devices, which correspond to the schematics in Figs. 2(d) and 2(f). In both devices, the waveguide width of cavity a is identical at 5.5 μm, with the critical difference lying specifically in the length difference between cavity b and cavity a. In Figs. 4(a) and 4(d), an increase in

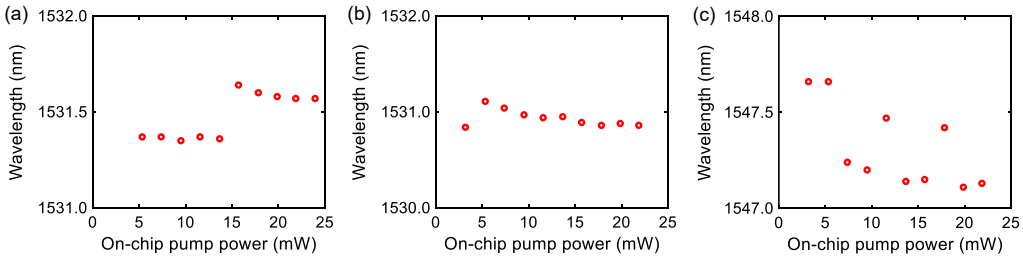

Fig. 5. Output laser wavelength drifts versus the pump power.

pump power correlates with a consistent rise in peak signal power, attaining 146 μW and 47.5 μW at a pump power of 22.9 mW, with associated laser signal wavelengths of 1530.85 nm and 1547.13 nm, respectively. The devices exhibit threshold pump powers of 5.1 mW and 2.59 mW, with respective slope efficiencies of 0.7% and 0.25%, as shown in Figs. 4(b) and 4(e). Both devices operate in a single mode across the spectral region from 1500 nm to 1580 nm, achieving high SMSR values of 32 dB and 40 dB, respectively, as evidenced in Figs. 4(c) and 4(f).

Figure 5 summarizes measurements of the laser wavelength drift versus pump power for the three different structural parameters of the devices. A general blue shift in the lasing wavelength is noted throughout the 1500–1580 nm spectrum with an increase in pump power. The alteration in resonance frequency with elevated pump power is chiefly ascribed to the photorefractive effect, which diminishes the cavity's refractive index, alongside mode gain competition. The reduction in refractive index directly leads to the observed blue shift.

In conclusion, a monolithic single-frequency nested dual-cavity microring laser has been realized on an Er^{3+}-doped TFLN platform. By utilizing the Vernier effect and gain competition, the laser achieves single-frequency operation with a maximum output power of 146 μW, a SMSR of 32 dB, and a slope efficiency of 0.7% at a wavelength of 1530.85 nm. Furthermore, precise adjustment of the device's structural parameters enables selective switching of the single-frequency lasing emission between 1530.85 nm and 1547.13 nm. Future research may utilize the electro-optic effect in TFLN to achieve enhanced control over laser signal modulation, facilitating unparalleled accuracy and tunability.

Acknowledgements. This work was supported by the National Key R&D Program of China (Grant No. 2024YFA1408900), the National Natural Science Foundation of China (Grant Nos. 12204176, 12192251, 12334014, 12404378, 12134001, 12174113, 12174107, 12474325, 12404379, and 12474378), Quantum Science and Technology-National Science and Technology Major Project (Grant No. 2021ZD0301403), and Shanghai Municipal Science and Technology Major Project (Grant No. 2019SHZDZX01).

References

[1] Weis R S and Gaylord T K 1985 *Appl. Phys. A* **37** 191
[2] Zhu D, Shao L, Yu M, Cheng R, Desiatov B, Xin C J, Hu Y, Holzgrafe J, Ghosh S, Shams-Ansari A, Puma E, Sinclair N, Reimer C, Zhang M, and Lončar M 2021 *Adv. Opt. Photonics* **13** 242
[3] Boes A, Corcoran B, Chang L, Bowers J, and Mitchell A 2018 *Laser Photonics Rev.* **12** 1700256
[4] Lin J, Yao N, Hao Z, Zhang J, Mao W, Wang M, Chu W, Wu R, Fang Z, Qiao L, Fang W, Bo F, and Cheng Y 2019 *Phys. Rev. Lett.* **122** 173903
[5] Shao L, Yu M, Maity S, Sinclair N, Zheng L, Chia C, Shams-Ansari A, Wang C, Zhang M, Lai K, and Lončar M 2019 *Optica* **6** 1498
[6] Wang C, Zhang M, Chen X, Bertrand M, Shams-Ansari A, Chandrasekhar S, Winzer P, and Lončar M 2018 *Nature* **562** 101
[7] He M, Xu M, Ren Y, Jian J, Ruan Z, Xu Y, Gao S, Sun S, Wen X, Zhou L, Liu L, Guo C, Chen H, Yu S, Liu L, and Cai X 2019 *Nat. Photonics* **13** 359
[8] Zhang M, Buscaino B, Wang C, Shams-Ansari A, Reimer C, Zhu R, Kahn J M, and Lončar M 2019 *Nature* **568** 373
[9] Wu T H, Ledezma L, Fredrick C, Sekhar P, Sekine R, Guo Q, Briggs R M, Marandi A, and Diddams S A 2024 *Nat. Photonics* **18** 218
[10] McKenna T P, Stokowski H S, Ansari V, Mishra J, Jankowski M, Sarabalis C J, Herrmann J F, Langrock C, Fejer M M, and Safavi-Naeini A H 2022 *Nat. Commun.* **13** 4532
[11] Jia Y, Wu J, Sun X, Yan X, Xie R, Wang L, Chen Y, and Chen F 2022 *Laser Photonics Rev.* **16** 2200059
[12] Cai M, Li T, Zhang X, Zhang H, Wang L, Li H, Zheng Y, Chen X, Chen J, and Wu K 2024 *ACS Photonics* **11** 4923
[13] Huang Q, Song H, Fang Z, Wang Z, Song L, Song Y, Yu J, Wang M, and Cheng Y 2025 *Laser Photonics Rev.* (in press)
[14] Bao R, Fang Z, Liu J, Liu Z, Chen J, Wang M, Wu R, Zhang H, and Cheng Y 2025 *Laser Photonics Rev.* **19** 2400765
[15] Chen Z, Xu Q, Zhang K, Wong W H, Zhang D L, Pun E Y B, and Wang C 2021 *Opt. Lett.* **46** 1161
[16] Luo Q, Bo F, Kong Y, Zhang G, and Xu J 2023 *Adv. Photonics* **5** 034002
[17] He X, Ma D, Zhou C, Xiao M, Chen W, and Zhou Z 2024 *Photonics Res.* **12** 1067
[18] Liu Y, Yan X, Wu J, Zhu B, Chen Y, and Chen X 2020 *Sci. China Phys. Mech* **64** 234262
[19] Zhang R, Yang C, Hao Z, Jia D, Luo Q, Zheng D, Liu H, Yu X, Gao F, Bo F, Kong Y, Zhang G, and Xu J 2021 *Sci. China Phys. Mech* **64** 294216
[20] Gao R, Guan J, Yao N, Deng L, Lin J, Wang M, Qiao L, Wang Z, Liang Y, Zhou Y, and Cheng Y 2021 *Opt. Lett.* **46** 3131
[21] Liu X, Chen C, Ge R, Wu J, Chen X, and Chen Y 2025 *Nano Lett.* **25** 6454
[22] Wu J, Yan X, Wang X, Yuan T, Chen C, Li H, Chen Y, and Chen X 2024 *ACS Photonics* **11** 2114
[23] Lin J, Farajollahi S, Fang Z, Yao N, Gao R, Guan J, Deng L, Lu T, Wang M, Zhang H, Fang W, Qiao L, and Cheng Y 2022 *Adv. Photonics* **4** 036001

[24] Li T, Wu K, Cai M, Xiao Z, Zhang H, Li C, Xiang J, Huang Y, and Chen J 2021 *APL Photonics* **6** 101301
[25] Luo Q, Hao Z, Yang C, Zhang R, Zheng D, Liu S, Liu H, Bo F, Kong Y, Zhang G, and Xu J 2020 *Sci. China Phys. Mech* **64** 234263
[26] Yu S, Fang Z, Wang Z, Zhou Y, Huang Q, Liu J, Wu R, Zhang H, Wang M, and Cheng Y 2023 *Opt. Lett.* **48** 2660
[27] Huang Q, Fang Z, Wang Z, Zhu Y, Liu J, Zhou Y, Yu J, Wang M, and Cheng Y 2025 *Photonics Res.* **13** 935
[28] Ma Y, Li M, Yu J, Fang Z, Wang M, Lin J, Zhang H, and Cheng Y 2025 *Nanophotonics* **14** 4703
[29] Han J, Li M, Wu R, Yu J, Gao L, Fang Z, Wang M, Liang Y, Zhang H, and Cheng Y 2025 *Opto-Electron. Sci.* **4** 250004
[30] Ma R M, Oulton R F, Sorger V J, Bartal G, and Zhang X 2011 *Nat. Mater.* **10** 110
[31] Liu W, Li M, Guzzon R S, Norberg E J, Parker J S, Lu M, Coldren L A, and Yao J 2017 *Nat. Commun.* **8** 15389
[32] Feng L, Wong Z J, Ma R M, Wang Y, and Zhang X 2014 *Science* **346** 972
[33] Hodaei H, Miri M A, Heinrich M, Christodoulides D N, and Khajavikhan M 2014 *Science* **346** 975
[34] Claes T, Bogaerts W, and Bienstman P 2010 *Opt. Express* **18** 22747
[35] Wang Y Y, Xu C X, Jiang M M, Li J T, Dai J, Lu J F, and Li P L 2016 *Nanoscale* **8** 16631
[36] Shang L, Liu L, and Xu L 2008 *Opt. Lett.* **33** 1150
[37] Wu R, Zhang J, Yao N, Fang W, Qiao L, Chai Z, Lin J, and Cheng Y 2018 *Opt. Lett.* **43** 4116
[38] Wu R, Wang M, Xu J, Qi J, Chu W, Fang Z, Zhang J, Zhou J, Qiao L, Chai Z, Lin J, and Cheng Y 2018 *Nanomaterials* **8** 910
[39] Hosseini E S, Yegnanarayanan S, Atabaki A H, Soltani M, and Adibi A 2010 *Opt. Express* **18** 2127
[40] Yariv A 2000 *Electron. Lett.* **36** 321